

Citation: Foelsche U., and G. Kirchengast: Sensitivity of GNSS Occultation Profiles to Horizontal Variability in the Troposphere: A Simulation Study, in: Occultations for Probing Atmosphere and Climate (G. Kirchengast, U. Foelsche, A.K. Steiner, eds.), Springer, Berlin-Heidelberg, 127-136, 2004.

Sensitivity of GNSS Occultation Profiles to Horizontal Variability in the Troposphere: A Simulation Study

U. Foelsche and G. Kirchengast

Institute for Geophysics, Astrophysics, and Meteorology (IGAM),
University of Graz, Graz, Austria.
ulrich.foelsche@uni-graz.at

Abstract. We investigated the sensitivity of atmospheric profiles retrieved from Global Navigation Satellite System (GNSS) radio occultation data to atmospheric horizontal variability errors. First, the errors in a quasi-realistic horizontally variable atmosphere relative to errors in a spherically symmetric atmosphere were quantified based on an ensemble of about 300 occultation events. This investigation was based on simulated data using a representative European Centre for Medium-Range Weather Forecasts (ECMWF) T511L60 analysis field with and without horizontal variability. Biases and standard deviations are, below 20 km, significantly smaller under a spherical symmetry assumption than corresponding errors in an atmosphere with horizontal variability. The differences are most pronounced below ~ 7 km height. Second, we assessed the relevance of either assuming the “true” profile vertically at a mean event location (the common practice) or along the actual 3D tangent point trajectory. Standard deviation and bias errors decrease significantly if the data are exploited along the tangent point trajectory. Third, the sensitivity of retrieval products to the angle-of-incidence of occultation rays relative to the boresight direction of the receiving antenna (aligned with the orbit plane of the Low Earth Orbit satellite) was analyzed based on the same ensemble of events for three different angle-of-incidence classes (0–10 deg, 20–30 deg, 40–50 deg; ensembles of about 100 events in each class). Below about 7 km, most errors were found to increase with increasing angle of incidence. Dry temperature biases between 7 km and 20 km exhibit no relevant increase with increasing angle of incidence, which is favorable regarding the climate monitoring utility of the data.

1 Introduction

The EGOPS4 software tool (End-to-end GNSS Occultation Performance Simulator, version 4) was used to generate simulated phase measurements and retrievals of the observables bending angle, refractivity, total air pressure, geopotential height, and (dry) temperature. For a detailed description of EGOPS see Kirchengast (1998) and Kirchengast et al. (2002). Section 2 gives an overview of the experimental setup. Results on the sensitivity to horizontal variability are presented in section 3 and the relevance of the geometry of reference profiles is discussed in section 4. The results on sensitivity to angle-of-incidence are shown in section 5. Conclusions and an outlook are provided in section 6.

2 Experimental Setup

2.1 Geometry

We assumed a full constellation of 24 Global Positioning System (GPS) satellites as transmitters and a GRAS (GNSS Receiver for Atmospheric Sounding) sensor onboard the METOP satellite with a nominal orbit altitude of ~ 830 km (Silvestrin et al. 2000). With such a constellation, about 500 occultation rising and setting occultations per day can be obtained. We simulated measurements over a 24 hour period on September 15, 2001, the date of the ECMWF analysis field used in the forward modeling.

We collected occultation events in three different azimuth sectors relative to the boresight direction of the receiving antenna. A schematic illustration of this division into several “angle-of-incidence” sectors is given in the left panel of Figure 1, while Table 1 summarizes the simulation design in terms of numbers of events simulated per sub-sector defined. With restriction to the described azimuth sectors we obtained a total of 306 occultation events during the selected 24 hour period. The geographic distribution is shown in the right panel of Figure 1. We obtained uniform distribution in latitude as well as equal density over oceans and over continents in each sector.

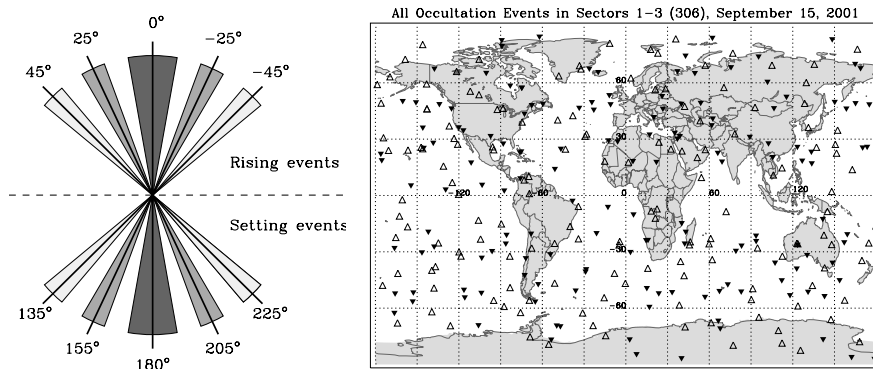


Fig. 1. Left panel: Schematic illustration of azimuth sectors used in the study: sector 1 (dark gray), sector 2 (medium gray), and sector 3 (light gray). Right panel: Locations of occultation events during one day in all three azimuth sectors. Upright open triangles denote rising occultations while upside-down filled triangles denote setting occultations.

Table 1. Number of occultation events in the three azimuth sectors used in this study.

	Sector 1	Sector 2	Sector 3	No. of events
Rising events	0° to -10°	-20° to -30°	-40° to -50°	76
	0° to +10°	+20° to +30°	+40° to +50°	76
Setting events	170° to 180°	150° to 160°	130° to 140°	77
	180° to 190°	200° to 210°	220° to 230°	77
No. of events	105	114	87	306

2.2 Forward Modeling

High resolution (T511L60) analysis fields from the European Centre for Medium-Range Weather Forecasts (ECMWF) for September 15, 2001, 12 UT, were used to generate quasi-realistic atmospheric phase delays. The horizontal resolution (T511) corresponds to 512×1024 points in latitude and longitude, respectively, and thus furnishes about eight or more grid points within the typical horizontal resolution of an occultation event of ~ 300 km (e.g., Kursinski et al. 1997). This dense sampling is important to have a sufficient representation of horizontal variability errors in occultation measurements. In the vertical, 60 levels (L60, hybrid pressure coordinates) extend from the surface to 0.1 hPa, being most closely spaced in the troposphere, which represents good vertical resolution. In order to illustrate the resolution of the T511L60 fields utilized, typical slices of temperature and specific humidity are displayed in Figure 2. The MSIS climatological model (Hedin 1991) was used, with a smooth transition, above the vertical domain of the ECMWF analysis field (from ~ 60 km upwards).

As we focused on the troposphere, we made the reasonable assumption that ionospheric residual errors can be neglected below 20 km (Steiner et al. 1999). Forward modeling was thus employed without the ionosphere, which corresponds to considerable savings in computational expenses. We performed high-precision 3D ray tracing with sub-millimeter accuracy and a sampling rate of 10 Hz for all forward modeled events through the ECMWF analysis (refractivity) field. In order to address the effects of horizontal variability, two separate ensembles of 306 events were forward modeled: One employing the analysis field with its 3D structure as is, the other by artificially enforcing spherical symmetry for each event. The latter case was obtained by using the refractivity profile at the mean tangent point of an occultation event (estimated between 12 and 15 km altitude) over the entire domain probed. As in the real atmosphere, occultation events over oceans at low latitudes occasionally failed to penetrate the lowest $\sim 2\text{--}4$ km of the troposphere, if the ray tracer encountered super-refraction or closely such conditions.

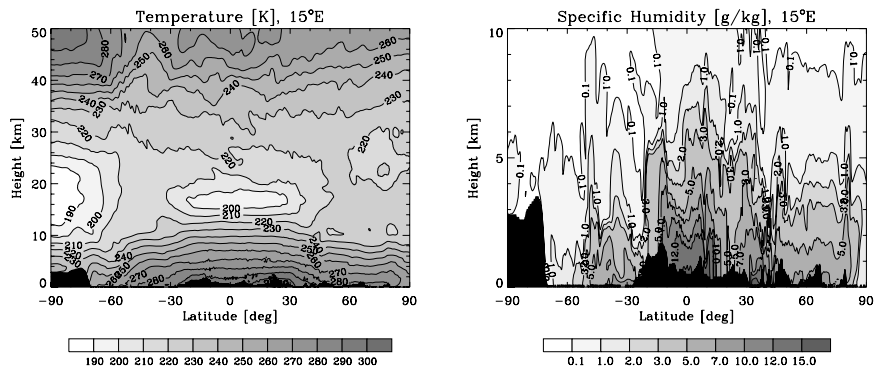


Fig. 2. Latitude-versus-Height slices at 15° eastern longitude; September 15, 2001, 12 UT (T511L60 ECMWF analysis fields). Left panel: temperature [K], right panel (different height range): specific humidity [g/kg].

2.3 Observation System Modeling and Retrieval Processing

Realistic errors (including error sources like orbit uncertainties, receiver noise, local multipath errors and clock errors) have been superimposed on the obtained simulated phase measurements. For this receiving system simulation, we used (conservatively) the specifications and error characteristics of the GRAS instrument (e.g., Silvestrin et al. 2000).

Regarding retrieval processing, we applied a geometric optics bending angle retrieval scheme. The core of this algorithm, transforming phase delays to bending angles, is the algorithm described by Syndergaard (1999), which was enhanced to include inverse covariance weighted statistical optimization (with prior best-fit a priori profile search) as described by Gobiet and Kirchengast (2002). Since the forward modeling has been performed without an ionosphere, ionospheric correction was omitted. Refractivity profiles have been computed using a standard Abel transform retrieval employing the algorithm of Syndergaard (1999). Profiles of total air pressure and of temperature have been obtained using a standard dry air retrieval algorithm as again developed by Syndergaard (1999). Geopotential height profiles were obtained by converting geometrical heights z of pressure levels via the standard relation $dZ = (g(z, \varphi)/g_0)dz$ (e.g., Salby 1996) to geopotential heights Z , where $g(z, \varphi)$ invokes the international gravity formula (e.g., Landolt-Börnstein 1984) and $g_0 = 9.80665 \text{ ms}^{-2}$ is the standard acceleration of gravity. We did not undertake to separately analyze temperature and humidity. For this baseline analysis of horizontal variability errors we decided to inspect variables such as refractivity and dry temperature, which do not require prior information.

2.4 Reference Profiles

All retrieved profiles have been differenced against the corresponding “true” ECMWF vertical profiles at the mean tangent point locations. The differences incurred by either assuming the reference profile vertically at a mean event location (the common practice) or more precisely along the estimated 3D tangent point trajectory has been assessed as well.

We compare to “true” (dry) geopotential height and dry temperature profiles from the ECMWF fields. This implies that the temperature profiles have an increasing moisture effect below 10 km. The dependence of dry temperature on actual temperature and humidity is accurately known, however, so that one can always determine the influence of moisture if desired.

3 Sensitivity to Horizontal Variability

While the analyses have been carried out for all described parameters we will focus here on discussing geopotential height and temperature errors only. In Figure 3, the results for the “real” atmosphere with horizontal variability (top panels)

are compared with the results for the artificial spherically symmetric atmosphere (middle panels). Furthermore, we computed errors by comparing with the “true” profiles extracted along the 3D tangent point trajectories (bottom panels). The statistical results for the full ensemble of 306 events are illustrated in each panel. The bias errors and standard deviations have been empirically estimated by differencing of retrieved profiles with co-located reference profiles. The gradual decrease in the number of events towards lower tropospheric levels (small left-hand-side subpanels) is due to the different minimum heights reached by individual events.

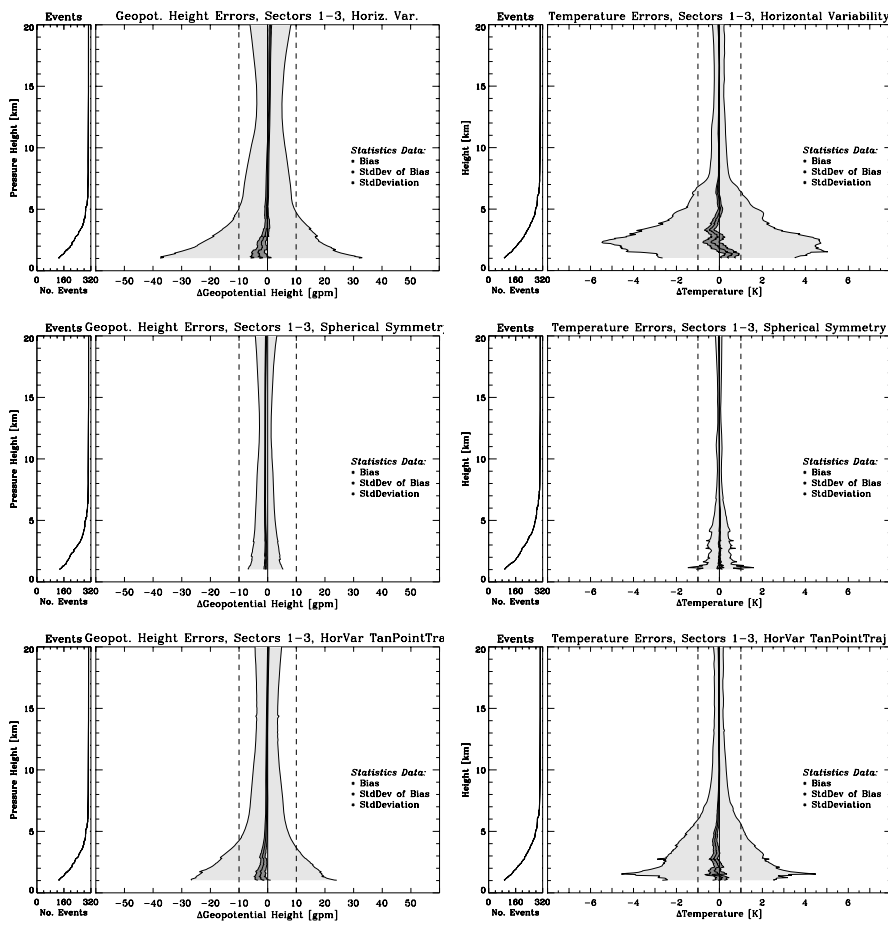


Fig. 3. Geopotential height (left) and Temperature (right) error statistics for the ensemble of all 306 occultation events. Top panels: atmosphere with horizontal variability; middle panels: atmosphere with spherical symmetry applied; bottom panels: horizontal variability with profile along 3D tangent point trajectory as reference. Sub-panels: number of events entering the statistics at a given height versus height.

3.1 Geopotential Height Errors

Errors in the geopotential height of pressure surfaces are shown in the left panels of Figure 3 as function of pressure height z_p (defined as $z_p = -7 \cdot \ln(p[\text{hPa}]/1013.25)$), which is closely aligned with geometrical height z . We note that geopotential height errors mirror pressure errors (not shown), i.e., positive biases in geopotential height correspond to negative biases in pressure (see, e.g., Syndergaard, 1999).

In the horizontally variable atmosphere (top panel) standard deviations above 5 km are smaller than 10 gpm (geopotential meters) while reaching 35 gpm at 1 km. Biases are generally negligible and bias values of more than 1 gpm are only found below 3 km. With reference profiles along the 3D tangent point trajectory (bottom panel), standard deviations remain smaller than 10 gpm down to 4 km and do not exceed 25 gpm at 1 km; biases are similarly small as in the top panel case. Under spherical symmetry (middle panel), biases never exceed 1 gpm, and standard deviations reach 6 gpm only at the lowest height levels.

3.2 Temperature Errors

The dry temperature errors are depicted in the right panels of Figure 3. In the scenario with horizontal variability (top panel), the errors are significantly larger than the corresponding errors under spherical symmetry.

Under horizontal variability, the bias reaches -0.5 K near 3.3 km and $+0.6$ K near 1.4 km, respectively, while standard deviations exceed 5 K near 2.3 km height. Comparing with reference profiles along the 3D tangent point trajectory (bottom panel) reduces the maximum bias by a factor of ~ 2 and the height where a standard deviation of 1 K is reached is lowered by about 1 km. Under spherical symmetry, the bias is smaller than 0.1 K everywhere, standard deviations remain smaller than 1 K with the exception of a small height interval below 1.5 km near the lower bound. Between 7 km and 20 km there is essentially no temperature bias in all scenarios (i.e., always smaller than 0.1 K).

4 Dependence on Geometry of Reference Profiles

Figure 4 (left panel) illustrates that differences between “true” vertical profiles at mean tangent point locations and “true” ones along actual 3D tangent point trajectories are fairly small at tropopause/lower stratosphere heights, since the EGOPS mean location estimate is designed to fit best near 12-15 km. Below 7 km, however, the differences are comparable to the errors estimated under horizontal variability (top left panel in Figure 3). This implies that the geometrical mis-alignment of the actual tangent point trajectory with the mean-vertical contributes as an important source to horizontal variability errors. Overall, the results show that the performance in the horizontally variable troposphere is markedly improved if measured against the actual tangent point trajectory.

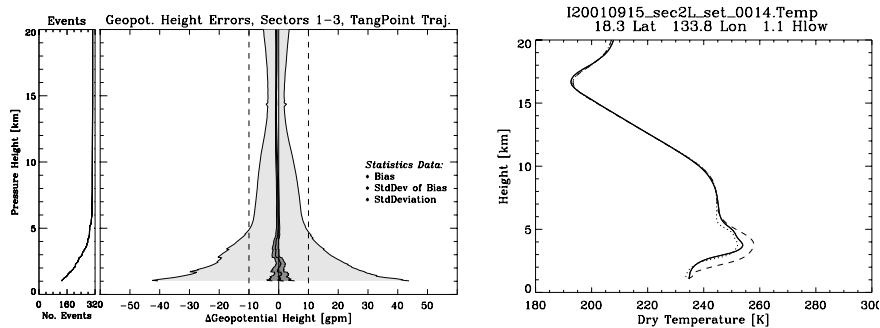


Fig. 4. Left panel: Differences between vertical reference profiles at the mean tangent point location and profiles along the 3D tangent point trajectory. Sub-panel: number of events versus height. Right panel: Typical dry temperature profile under high horizontal variability: retrieved profile (solid), reference profile at mean tangent point location (dashed), and reference profile along the 3D tangent point trajectory (dotted), respectively.

It should be noted that the exact trajectory cannot be determined without performing ray tracing. To a high degree of accuracy, however, it can be estimated from observed data (GNSS and LEO satellite positions and bending angles). Future work will thus investigate by how much the applicable standard deviations and bias errors decrease if the data are exploited along a tangent point trajectory deduced purely from observed data.

The right panel of Figure 4 shows a typical temperature retrieval in an area with high horizontal variability. In this cases, the two types of reference temperature profiles differ by several Kelvins and the retrieved profile is clearly much closer to the 3D tangent point reference profile than to the vertical one.

5 Sensitivity to the Angle-of-Incidence

In this section the sensitivity of retrieval products to the angle-of-incidence of occultation rays relative to the boresight direction of the receiving antenna (aligned with the LEO orbit plane) is analyzed. Error analyses have been performed for each azimuth sector defined in section 2.1 (ensembles of 105, 114, and 87 events, respectively), for every atmospheric parameter under study. We show again results for geopotential height and temperature errors only.

Events in sector 1 are associated with almost co-planar GNSS and LEO satellites, which should lead to the most-vertical and best-quality occultation events. We would thus expect an increase of errors with increasing angle of incidence. Figure 5 shows the results for sector 1 in the top panels, for sector 2 in the middle panels, and for sector 3 in the bottom panels, respectively.

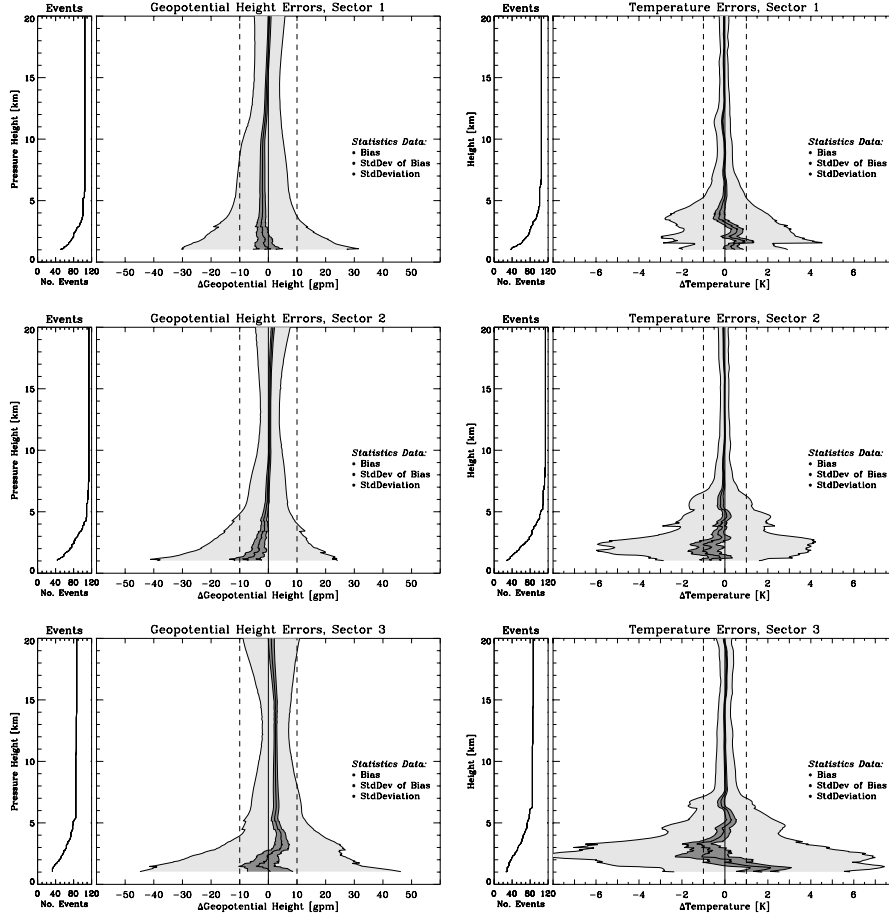


Fig. 5. Geopotential height (left) and Temperature (right) error statistics for the different azimuth sectors. Top panels: sector 1; middle panels: sector 2; bottom panels: sector 3. Sub-panels: number of events versus height.

5.1 Geopotential Height Errors

Errors in the geopotential height of pressure surfaces are shown in the left panels of Figure 5, again as function of pressure height (cf. section 3.1). While standard deviations generally increase with increasing angle of incidence, the behavior of the bias profiles is more complex and interesting. Between ~ 3 and ~ 18 km we find the smallest biases in sector 2, events in this sector are close to bias-free between 5 and 18 km altitude (bias < 1 gpm).

In sector 1, on the one hand, there is an almost constant negative bias of ~ 2 gpm between ~ 2 and ~ 10 km, while in sector 3, on the other hand, we find an

almost constant positive bias of ~ 2.5 gpm between ~ 5 and ~ 15 km. In the ensemble of all events (see Sect. 3.1) this adds (together with a smaller number of events in sector 3) to very small biases down to about 3 km. Though biases as small as up to 2.5 gpm are not a real concern, we are currently investigating these datasets closer in order to understand the causes of this subtle behavior.

5.2 Temperature Errors

The dry temperature errors are shown in the right panels of Figure 5. Their general behavior is more in line with expectations than that of geopotential height errors.

Below 7 km, biases and standard deviations increase significantly with increasing angle of incidence. Standard deviations in sector 1 (azimuth $0-10^\circ$) have maximum values of 3.7 K, those in sector 2 (azimuth $20-30^\circ$) reach 5.0 K, and those in sector 3 (azimuth $40-50^\circ$) even 8.0 K. Biases in sectors 1 and 2 remain smaller than 0.9 K and 1.1 K, respectively, while they reach about 2 K in sector 3.

Biases between 7 km and 20 km are smaller than ~ 0.1 K and exhibit no relevant increase with increasing angle of incidence. Standard deviations in the same height interval remain smaller than 0.5 K (except close to 7 km), those in sector 3 are only slightly larger than respective errors in sector 1 and sector 2.

6 Summary and Conclusions

We investigated the sensitivity of atmospheric profiles retrieved from GNSS radio occultation data to atmospheric horizontal variability errors, based on an ensemble of about 300 simulated events. Biases and standard deviations are, below 20 km, significantly smaller under a spherical symmetry assumption than corresponding errors in a quasi-realistic atmosphere with horizontal variability. The differences are most pronounced below ~ 7 km height. Temperature standard deviations, for example, remain smaller than 1 K in a spherically symmetric atmosphere, while they reach values of about 5 K in the horizontally variable atmosphere. This confirms earlier results based on a more simplified estimation by Kursinski et al. (1997), that horizontal variability is an important error source in the troposphere. Dry temperature profiles between 7 km and 20 km were found to be essentially bias-free in both the horizontal variability and spherical-symmetry scenarios (biases smaller than 0.1 K), which confirms the unique climate monitoring utility of GNSS occultation data.

A significant part of the total error below ~ 7 km can be attributed to adopting reference profiles vertically at mean tangent point locations instead of extracting them along actual 3D tangent point trajectories through the troposphere. Future work will investigate by how much the standard deviation and bias errors decrease if a tangent point trajectory deduced purely from observed data is used instead.

Below about 7 km most errors were found to increase with increasing angle of incidence. This is in line with the hypothesis that larger angles of incidence lead to

more sensitivity to horizontal variability. Geopotential height biases in the 20–30 deg azimuth sector above ~3 km, however, are smaller than corresponding biases in the 0–10 deg sector, which merits further investigation. In general, the sensitivity of bias errors to increases of the angle of incidence has been found to be relatively small, which is favorable regarding the climate monitoring utility of the data. For example, dry temperature biases between 7 km and 20 km exhibit no relevant increase with increasing angle of incidence. Current cautionary approaches restricting the events used in climate studies to small angles of incidence (such as < 15 deg; Steiner et al. 2001) appear thus to be overly conservative and can be safely relaxed to using the data at least up to 30 deg.

Acknowledgements. The authors gratefully acknowledge valuable discussions on the topic with A.K. Steiner (IGAM, Univ of Graz, Austria) and S. Syndergaard (IAP, Univ of Arizona, Tucson, USA). U.F. was funded for this work from the START research award of G.K. financed by the Austrian Ministry for Education, Science, and Culture and managed under Program Y103-CHE of the Austrian Science Fund.

References

- Gobiet A, Kirchengast G (2002) Sensitivity of atmospheric profiles retrieved from GNSS occultation data to ionospheric residual and high-altitude initialization errors. Tech Rep ESA/ESTEC-1/2002, IGAM/Univ of Graz, Austria, 56 pp
- Hedin AE (1991) Extension of the MSIS thermosphere model into the middle and lower atmosphere. *J Geophys Res* 96: 1159–1172
- Kirchengast G (1998) End-to-end GNSS Occultation Performance Simulator overview and exemplary applications. *Wissenschaftl Ber* 2/1998, IGAM/Univ Graz, Austria, 138 pp
- Kirchengast G, Fritzer J, Ramsauer J (2002) End-to-end GNSS Occultation Performance Simulator version 4 (EGOPS4) software user manual (overview and reference manual), Tech Rep ESA/ESTEC-3/2002, IGAM/Univ of Graz, Austria, 472 pp
- Kursinski ER, Hajj GA, Schofield JT, Linfield RP, Hardy KR (1997) Observing Earth's atmosphere with radio occultation measurements using the Global Positioning System, *J Geophys Res* 102: 23,429–23,465
- Landolt-Börnstein (1984) *Geophysics of the Solid Earth, the Moon and the Planets – Numerical data and functional relationships in science and technology*, vol. V/2a (K Fuchs and H Stoffel, Eds), Springer Verlag, Berlin–Heidelberg, 332–336
- Salby ML (1996) *Fundamentals of Atmospheric Physics*, Academic Press, San Diego
- Silvestrin P, Bagge R, Bonnedal M, Carlström A, Christensen J, Hägg M, Lindgren T, Zangerl F (2000) Spaceborne GNSS radio occultation instrumentation for operational applications, Proc 13th ION-GPS Meeting 2000, Salt Lake City, UT, USA
- Steiner AK, Kirchengast G, Ladreiter HP (1999) Inversion, error analysis, and validation of GPS/MET occultation data. *Ann Geophys* 17: 122–138
- Steiner AK, Kirchengast G, Foelsche U, Kornblüh L, Manzini E, Bengtsson L (2001) GNSS occultation sounding for climate monitoring. *Phys Chem Earth A* 26: 113–124
- Syndergaard S (1999) Retrieval analysis and methodologies in atmospheric limb sounding using the GNSS radio occultation technique. DMI Scient Rep 99-6, Danish Meteorological Institute, Copenhagen, Denmark, 131 pp